Towards Imaging-based Digital Design of Complex Functional Composites

Denis Kramer*, Joshua Simons, Thomas Carraro, Jens Wulfsberg, …
Helmut-Schmidt-University / University of the Armed Forces
Hamburg, German
*d.kramer@hsu-hh.de

Claudio Pistidda*, Thomas Klassen, Maximilian Passing
Helmholtz Centre Hereon
Institute of Hydrogen Technologies
Geesthacht, Germany
*claudio.pistidda@hereon.de

Christina Krywka*, Julian P. Moosman, Imke Greving, Silja Flenner
Helmholtz Centre Hereon
Institute of Materials Physics
Hamburg, Germany
*christina.krywka@hereon.de

***Abstract* – Functional composites are ubiquitous in technology. They allow to simultaneously optimize functional properties against multiple application demands by combining several phases, each contributing desired functions. However, the forming structure and internal interfaces govern the overall properties of the composite in complex ways. Without understanding these complex structure-property relationships, rational design of advanced functional composites is impossible. Here we present new capabilities and ambitions of the CTCentre for Functional Composites, touching on infrastructure, advanced image processing, image-based modelling, as well as a selection of use cases and applications.**

Tomography, Imaging, Composites, Advanced Manufacturing, Hydrogen Storage

I. Introduction

Composite materials are indispensable for engineering innovation. They are found in buildings (e.g, concrete), structural components of machines (e.g., carbon fibre composites) and energy storage and conversion devices (e.g., battery electrodes) to name only a few. Fundamentally, they promise to comply with complex, multi-dimensional demand-metrics by combining multiple phases, each addressing one or more of the material requirements. Typical requirements are material strength, low/high weight, high/low heat/mass transport, activity for chemical reactions and so on. In each of these cases, the emerging macroscopic properties are not only a function of the phases; they critically depend on the morphology (i.e., the distribution and interconnectivity of the phases in a composite) as well.

Hence, measuring the morphology of a composite is the first step to understand its behaviour. Todays advanced X-ray tomography platforms provide powerful, experimental access to the internal structure of composite materials. Lab-based systems provide millimetre to sub-micrometre resolution, which is well suited for a large range of composite materials. However, composites also commonly comprise structural features at the nanometre scale that demand highest resolution at synchrotron-based facilities. In addition, composite materials are often hierarchical in the sense that structural features span several orders of magnitude. Concrete is a good example: cement pastes typically have pore sizes in the micrometre range, while aggregates are millimetre to centimetre in size. This typically calls for a combination of imaging approaches to fully resolve structural features across all relevant length scales.

Finally, composite morphology needs to be mapped to macroscopic properties to be useful in the design of functional materials. Digital approaches to constructing these structure-property relationships are attractive to minimize the need for time consuming and costly series of experiments. Common approaches include direct numerical simulation of physical phenomena [1], mathematical homogenization approaches [2] as well as the use of machine learning [3].

Hence, an integrated approach that combines CTs, capable of resolving all relevant length-scales, with advanced data management and simulation capabilities is desirable to digitally map the structure-property relationships and accelerate design and innovation cycles.

II. Infrastructure

A. X-Ray Tomography Platforms

The DTEC.Bw CTCentre builds on two X-ray tomography facilities housed at the Helmut-Schmidt-University and a

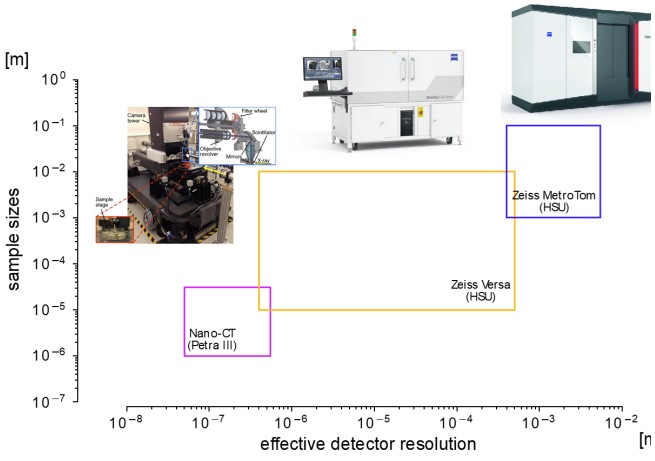

Figures 1: Effective resolution and sample sizes of X-Ray tomography platforms.

synchrotron-based platform at PETRA III in Hamburg, spanning sample sizes from tens of microns to tens of centimetres and resolutions from nanometres to millimetres (cf. FIGURE 1).

Moving large voxel sets, which can easily exceed 60 GB each, from storage to compute infrastructure and back is increasingly becoming a true bottleneck in processing tomography data. Early test data, using a single storage server and ten client nodes communicating via InfiniBand, indicates

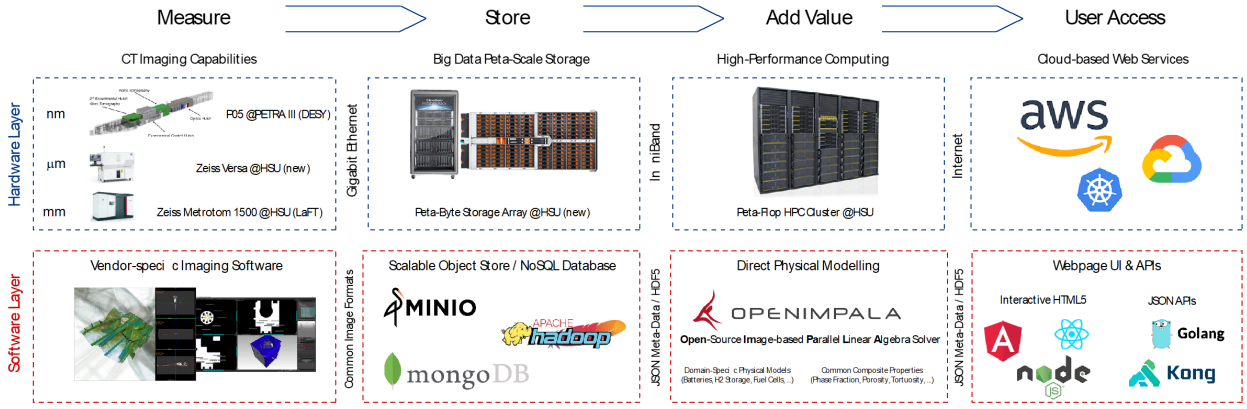

FIGURE 2: DIGITAL INFRASTRUCTURE FOR SCALABLE STORAGE AND EFFICIENT PROCESSING OF LARGE DATASETS

The two commercial, lab-based systems supplied by Zeiss provide resolution from sub-microns upwards and can image sample sizes of a few millimetre up to several tens of centimetres. The Zeiss Versa 620 produces X-rays powerful enough to penetrate several millimetre of metal whilst retaining excellent resolution across a range of X-ray energies. It is well suited to imageing samples with dimensions in the millimetre to centimetre range and resolves structural features in the micrometre domain (e.g., batteries, fuel cells, metal hydride samples, carbon fibre composites, …). The Zeiss MetroTom provides even higher energy x-rays capable of penetrating centimetres of metal and resolves internal features with sub-millimetre resolution. It is well suited to imageing samples with dimensions in the centimetre range (e.g., structural components, metal foams, additive manufacturing products, …).

A full-field X-ray microscope has been installed at the nanotomography end station at the imaging beamline P05 at the PETRA III storage ring at DESY, which is operated by the Helmholtz-Zentrum Hereon [4]. The transmission X-ray microscopy can be operated in standard absorption, Zernike phase contrast and near-field holotomography mode and offers a high temporal resolution with tomographic scan times down to 6 s and spatial resolutions below 100 nm.

B. *Data Storage and Computing*

The ability to store and manipulate large datasets is fundamental to the centres ambition. Further, meaningful scalability requires a high level of automation for storage, retrieval, compute and visualisation elements of data processing workflows. The centre implements a tiered digital infrastructure (cf. FIGURE 2) to address these requirements.

A key element is the co-location of a PetaByte object storage array with the new high-performance computing cluster (HPC) HSUper [5] at HSU. The storage array has direct access to the InfiniBand interconnect of the HPC cluster for maximal data throughout. The solution is based on Ceph [6], an open-source, distributed storage system with its own high-performance Rados API for distributed read/write access.

that the hardware side integration of the storage array with the HPC interconnect enables single throughput of a few GB/s in read and write with good scalability for concurrent read operations (cf. TABLE 1). The good scalability of the concurrent read operations highlights the benefits of a distributed storage strategy: there is no single point that all traffic has to pass through. This is an excellent match to the distributed compute model of distributed memory HPC clusters, where individual MPI processes operate on subsets of a larger compute task. Individual MPI processes can directly communicate with individual storage servers hosting relevant parts of the total dataset. The price that has to be paid for this I/O scalability is the need to custom-code the I/O operations of scientific software with the storage cluster using the Rados API provided by Ceph rather than a file system.

TABLE I: DATA THROUGHPUT OF A CEPH STORAGE TEST SETUP.

Single Write	*Random/Sequential Single Read*	*Concurrent 10x Write*	*Random/Sequential Concurrent 10x Read*
~1.1 GB/s	2.5 GB/s	~3.8 GB/s	~13.8 GB/s

It is a key ambition of the CTCentre to add value by overlaying tomographies with physical simulations to extract application relevant characteristics and properties, ideally in an automated way. Therefore, it is attractive to utilise HPC clusters and distributed compute strategies to directly compute on tomography voxel sets as these can be easily subdivided in space. However, this requires specialised codes developed with parallel computing in mind.

One such code is the Open-Source Image-based Parallel Linear Algebra Solver (OpenImpala) [7], which has been designed from the ground up to take advantage of parallel HPC environments to solve PDE-based models directly on voxel sets, circumventing the need for meshing, which is often a manual and error-prone task. OpenImpala has been ported and optimised to the new HPC infrastructure at HSU. FIGURE 3 shows a scaling analysis of a diffusive mass transport problem in random packings of spheres with domain sizes ranging from 10^6 to 10^8 voxels. These Poisson-type problems allow to extract important characteristics of

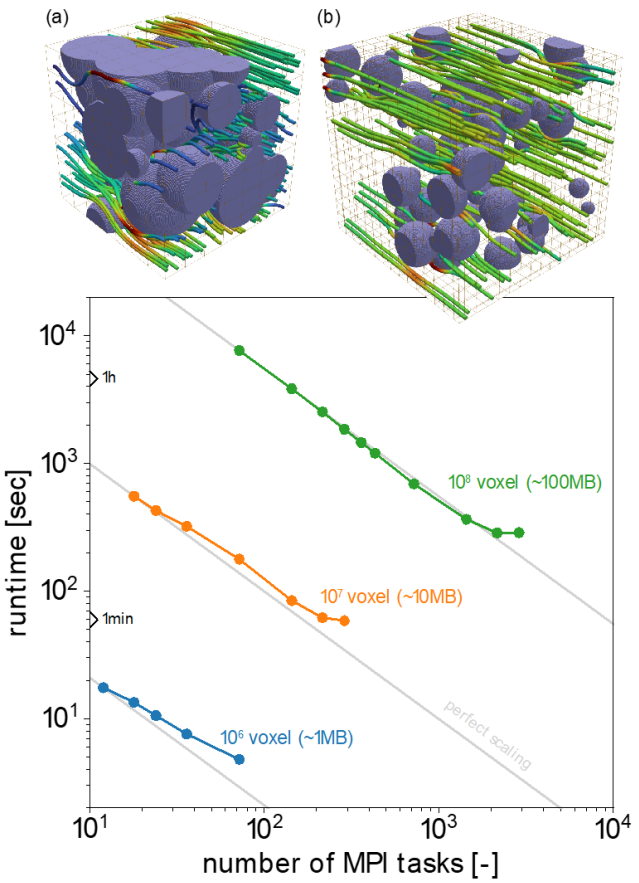

FIGURE 3: PARALLEL PERFORMANCE OF A DIFFUSIVE MASS TRANSPORT PROBLEM IN RANDOM SPHERES SOLVED ON HSUPER WITH OPENIMPALA; (A) DOMAIN WITH 10^7 VOXELS, (B) DOMAIN WITH 10^8 VOXELS; VALUES IN BRACKETS INDICATE DATASET SIZE ASSUMING AN 8BIT GRAYSCALE; LIGHT GRAY LINES VISUALIZE REDUCTION IN COMPUTE TIME WITH PERFECT PARALLELISATION.

composites such as effective transport parameters relevant for mass and heat transport, but also for elasticity problems. The computational domains comprising 10^7 and 10^8 voxels are shown in (a) and (b), respectively. Streamlines indicate the mass flux through the complex geometries with green/red representing low/high fluxes. The domains were subdivided into boxes, indicated by the brown grids lines, and the Poisson equation solved in parallel in each of these boxes utilising a varying number of processors (i.e., MPI tasks) on HSUper.

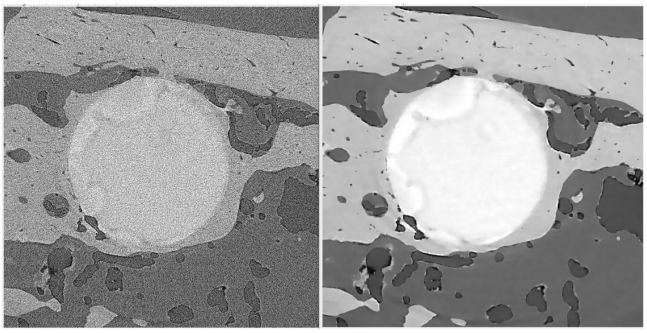

FIGURE 5: MACHINE-LEARNING BASED DENOISING OF AN ABSORPTION CONTRAST MICROTOMOGRAPHY SCAN OF A MG10GD IMPLANT IN BONE. LEFT: RECONSTRUCTION BEFORE DENOISING. RIGHT: DENOISED IMAGE USING DUAL DENOISING APPROACH WITH A NON-LOCAL MEANS FILTER APPLIED PRIOR TO NOISE2INVERSE.

The FIGURE 3 shows the required compute time for three voxel sets as a function of the number of utilised parallel processes. For larger voxel sets, OpenImpala shows almost perfect parallel performance up to the limit of one MPI process per box beyond which a reduction in compute time can only be expected by choosing smaller box sizes and more boxes, respectively.

Tomographic voxel sets can comprise up to 10^9 or even close to 10^{10} voxels due to the availability of CMOS detectors with 1024x1024 or 2048x2048 pixels. We expect to be able to directly solve Poisson-type problems on these very large domains within a matter of hours utilising around 2% of the available compute power at HSUper (i.e., 1000 cores). To put this into perspective, solving such problems on a domain comprising 10^8 voxels on a single CPU would almost take a week.

C. *Visualisation and Access*

Visualisation and data access is a vital part of the overall strategy to add value for external collaborators. These parts of the ecosystem will be implemented in a later phase of development and comprise APIs and web-interfaces to access and visualise tomography and simulation data alike.

III. APPLICATIONS AND USE CASES

A. *Advanced Image Processing*

1) *Machine-Learning for Noise reduction*

For in situ as well as high-throughput experiments, tomographic scan times are a limiting factor. Using a mixed-scale dense convolutional neural network [8], the noise in the

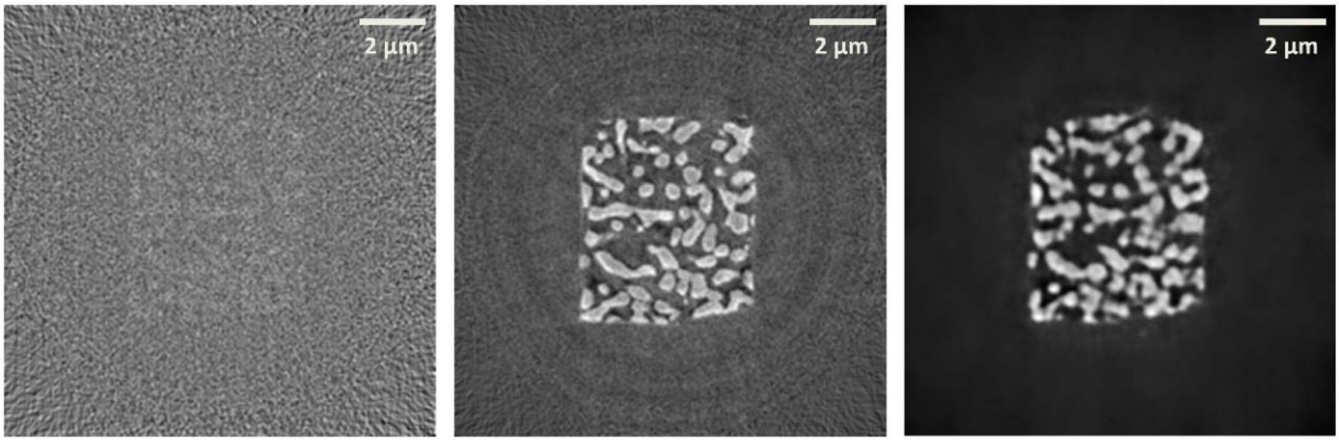

FIGURE 4: MACHINE-LEARNING BASED DENOISING OF NANOPOROUS GOLD WITH A BINARY STRUCTURE USING HIGH- AND LOW-QUALITY ABSORPTION CONTRAST NANOTOMOGRAPHY SCANS. LEFT: INPUT DATA FROM A FAST SCAN WITH VERY HIGH NOISE. MIDDLE: TARGET DATA FROM A LONG HIGH-QUALITY SCAN. RIGHT: DENOISED OUTPUT FROM THE NEURAL NETWORK. IMAGES TAKEN FROM [9].

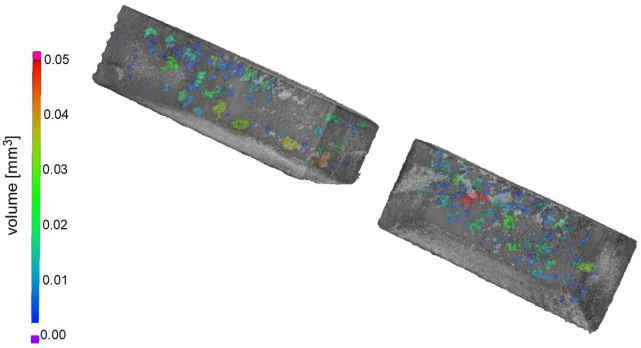

FIGURE 6: POROSITY IN A PRINTED STAINLESS STEEL SAMPLE; VOIDS ARE COLORED BY VOID VOLUME.

reconstructed tomogram could be reduced considerably or even eliminated. Here, a long high-quality scan is acquired before (or after) the *in situ* experiment and short scans during the *in situ* experiment. The network is then trained on a short and a corresponding long scan which acts as a ground truth, see FIGURE 4 where a nanoporous gold structure was scanned using absorption contrast nanotomography [9]. With this approach, fast scans in the order of about 3 min can produce a similar image quality as high-quality scans which take at least 15-30 min. The right image in FIGURE 4 shows that the noise is completely eliminated in the reconstruction. This is because the neural network learns the `real' structures and does not reproduce the random noise. Another unsupervised approach is Noise2Inverse where, assuming a sufficient number of projections have been acquired, the projections of a single tomographic scan are split in two independent stacks resulting in two reconstructions from the same measurement with identical sample information, but uncorrelated noise [10]. The Nosie2Inverse approach denoises images without introducing an additional blurring and allows to resolve fine structures down to very few pixels (cf. FIGURE 5).

2) Super-resolution

To understand the functional behaviour of composites, their microstructure must be studied, and imaging techniques are central in this area. However, composites are often heterogeneous and require quantification of small features over representative volumes. Therefore, resolution of microscopy image data is critical in the study of composites. Microscopy equipment is time consuming and expensive to operate, and resolution, i.e., the size of the acquired image voxel, is indirectly proportional to the volume of tomography. High resolution is required to capture small features of the composites but limits the maximum volume that can be imaged. Direct simulation at the microscopic level to model composite behaviour is not possible for macroscopic volumes. For example, spatially resolved models discretized with finite differences, as shown above can be solved numerically with voxels on the order of 10 nanometres only for volumes of a few micrometres. For this reason, multiscale models are essential to model functional properties at the macroscopic level. In the case of multiscale models, the calculations performed at the microscopic level need only be statistically representative. That is, they must be large enough to capture the typical variations within a macroscopic volume. Given the physical limitations of a tomographic technique, there is a trade-off between a large representative volume and well-resolved small features within that volume. Machine learning techniques can be used to overcome the inherent limitation of the imaging technique used, as recent work has shown [12]. These techniques are called super-resolution because they improve the resolution of tomographic images. Various machine learning techniques have been used for this purpose [12]. For example, in [13], the use of generative adversarial networks for crack detection in aged cathode particles of lithium ion cells was demonstrated. Different techniques for super-resolution of SEM data of cathode materials were compared. The neural networks used for super-resolution must be trained with high- and low-resolution data. It is shown that the high- and low-resolution data pairs do not have to match. In fact, using down-sampled images from high-resolution images is not the best way to perform super-resolution, as it is shown that artificially generated low-resolution images cannot be compared to measured low-resolution images. At the CTcenter, images with different resolution can be acquired taking full advantage of the CT platforms spanning several orders of resolution. Therefore, the investigation of super-resolution techniques using images acquired with different instruments is planned with the aim to reduce the demand for synchrotron-based measurements.

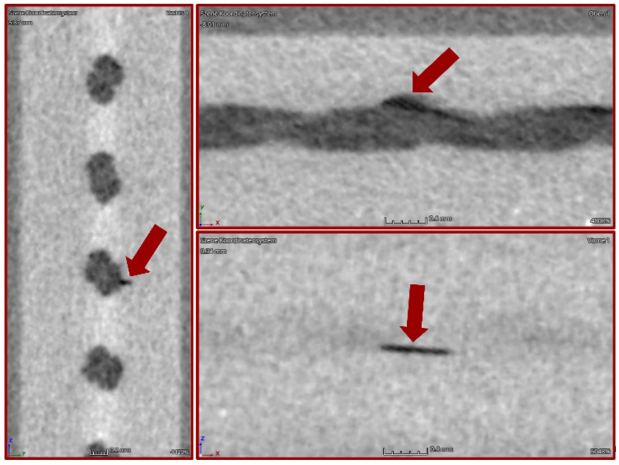

FIGURE 7: INTERFACE RUPTURE BETWEEN RUBBER AND CORD.

B. Technology Research

1) Advanced Manufacturing

Laser powder bed fusion (LPBF) is a popular additive manufacturing technique, where high power lasers fuse powdered alloys. X-Ray tomography enables the investigation of adhesion defects between the melt lines. An example of void detection in printed stainless steel is shown in FIGURE 6. Of special interest are the morphology, distribution, and quantity. Manufacturing results of laser powder bed fusion of metals are improved by researching the effect of process parameters on adhesion defects. Optimal process parameters result in samples without adhesion defects.

Defect detection and analysis of manufactured components after service life is another important area of interest. As an example, FIGURE 7 shows results of long-term cyclic tests of air spring sleeve configurations used in the automotuve industry. A defect formed after testing is marked by red arrows. Points of weakness can be identified with non-destructive X-ray imaging and provide hints for further improvement in manufacturing.

2) Hydrogen Storage

One of the most challenging tasks in designing a metal hydride tank is to achieve a good heat management of the

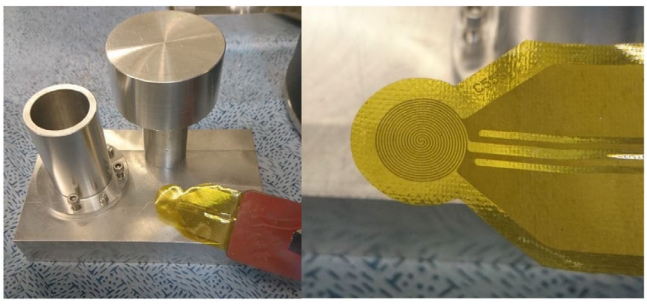

FIGURES 8: EXPERIMENTAL SETUP FOR THE TPS "HOT DISC" MEASUREMENTS (LEFT) AND THE USED KAPTON SENSOR (RIGHT)

whole system. Due to the endothermic desorption and the exothermic absorption, great amounts of heat must be transported inside and outside the powder bed, respectively. The heat transport inside a powder bed is described by the effective thermal conductivity. For investigating how the material particle sizes and particle shapes influence the material thermal conductivity, powders of the Mg alloy AZ91 were utilized as model systems. The thermal conductivity was measured through the hot disk transient plane source method (TPS 1500 from Hot Disk AB).

The as received Mg based alloy was milled under an argon atmosphere using a high-energy ball mill. The used mill is an industrial Simoloyer-CM08 ball mill (ZOZ GmbH). The milling time was set to two hours and the ball to powder ratio was 1:20. During the milling a speed program of a periodic repetition of 700 rpm for 30 s and 300 rpm for 30 s was chosen. Milling tools of 100Cr6 steel with a diameter of 5 mm were used. No other materials were added to the mill. Three batches of about 350 g Mg waste powder were produced. After milling the Mg based alloy, the powder was sieved for one hour in a sieving machine (Analysette 3 Pro from the company FRITSCH). The mesh sizes of 63 µm, 125 µm and 355 µm were chosen. The obtained powder fractions were labeled based on the average diameter of the particles (dp) as: 1) Batch 1 (B1) dp<63 μm; 2) Batch 2 (B2) 63 $\mu m \leq dp$<125 μm; 3) Batch 3 (B3) 125 $\mu m \leq dp$<355 μm; 4) Batch 4 (B4) 355 $\mu m \leq dp$. The effective thermal conductivity for the different powder batches B1–B4 is measured with isotropic and anisotropic settings. In FIGURE 8 the measured effective thermal conductivities are compared with each other. It is noticeable, that the isotropic measured results are in the same range for the batches B1–B3 of about 0.18 W/mK, whereas B4 has a more than twice as high thermal conductivity of 0.43 W/mK. This benchmark data will help to verify the image-based determination of effective transport parameters using the highly parallel Poisson solver provided by openImpala.

IV. CONCLUSION AND OUTLOOK

The CTCentre has already made significant strides towards image-based design of functional composites. The required digital infrastructure is in place and operational. Two of the three CT platforms are operational, and the remaining micro-CT will be delivered in the next months. Software assets such as OpenImpala or image-processing codes are currently under development or are integrated with the digital infrastructure. In the next phase, we look forward to complete the lab-based and digital infrastructure before shifting the focus towards applications and external access.

ACKNOLODGEMENT

This Paper is funded by dtec.bw – Digitalization and Technology Research Center of the Bundeswehr which we gratefully acknowledge [project CTCentre].

REFERENCES

[1] J. Le Houx, D. Kramer, *Energy Reports* **7** (2021) 9.

[2] A.L. Kalamkarov, *Appl. Mech. Rev.* **62**(3) (2009) 1.

[3] C. Qiu, J. Yang, *ACS Symp. Series* **1416**(4) *(2022) 65*.

[4] M. Ogurreck *et al. J. Phys. Conf. Ser.* **425** (2013) 182002; M. Ogurreck *et al.,* J. Phys. Conf. Ser. **849** (2017) 012056; S. Flenner *et al.*, *Microsc. Microanal.* **24** (2018). 148.

[5] https://www.hsu-hh.de/hpc/en/hsuper-2/.

[6] https://ceph.io

[7] J. Le Houx, D. Kramer, *SoftwareX* **15** (2021) 100729.

[8] D. Pelt, K. Batenburg, J. Sethian, *J. Imaging* **4** (2018) 128; D. Pelt, J. Sethian, *PNAS* **115** (2018) 254.

[9] S. Flenner *et al.*, J. Synchrotron Rad. **27** (2020). 1339.

[10] A. Hendriksen *et al.*, *IEEE Trans. Comput. Imaging* **6** (2020) 1320.

[11] Z. Wang *et al.*, *IEEE Trans. Pattern Anal. Mach. Intell.* **43** (2021) 3365.

[12] X. Yu, F. Porikli, *Proc. Europ. Conf. Comp. Vis.* (2016) 18; C. Ledig *et al.*, Proc. IEEE Conf. Comp. Vis. (2017) 105; L. Fan *et al.*, Nanomaterials **11** (2021) 3305.

[13] O. Furat *et al., npj Comput. Mater.* **8** (2022) 68.